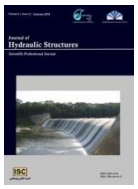
Journal of Hydraulic Structures
J. Hydraul. Struct., 2021; 7(2):72-99
DOI: 10.22055/JHS.2021.38072.1183



OPEN ACCESS

Combined SPH-DEM modeling of solid-fluid interactions

Mohsen Rajab Doost Khoshdel [1]
Ehsan Taheri [2]
Ali Fakhimi [3]

Abstract

Evaluation of Solid-Fluid interaction is of high significance in all engineering fields. In this paper, the Smoothed Particle Hydrodynamics (SPH) and the Discrete Element Method (DEM) were employed to simulate fluids and solids, respectively. As for the simulation of water behavior, first, a single-phase "dam break" experiment is modeled by the SPH. In this model, variable smoothing length and an almost novel boundary method were utilized which resulted in a tremendous boost in its resemblance to the experiment. To couple these methods (SPH and DEM), three approaches were proposed and validated against a famous experimental test named "dam break with an elastic gate test". Finally, to be sure of the correctness of these approaches, an elastic plate under a water column in the hydrostatic condition was simulated and the error was 2 percent in comparison with the analytical solution. In pursuit of having short run-times, parallel computing on GPU (CUDA) was employed, and a robust nearest neighbor search (NNS) algorithm was modified and developed.

Keywords: Discrete Element Method (DEM), Smoothed Particle Hydrodynamics (SPH), Fluid-Structure Interaction (FSI), Nearest Neighbor Search (NNS) algorithm, Parallel computing with GPU (CUDA)

Received: 25 July 2021; Accepted: 10 September 2021

1. Introduction

Understanding the nature of fluids and solids interactions is of high importance in almost all engineering fields. Thus, no matter how advanced the methods and measuring instruments are (or perhaps we think they are), there is still more room for improvement. These interactions are the case of interest in many subjects, such as trapping gas in rocks [1], blasting [2], water accumulation behind dams [3], flood [4], undrained tests [5] and blood flow in veins [6] to name but a few.

Over the past few decades, with the development of novel numerical techniques like Finite

[1] Faculty of Engineering, Tarbiat Modares University, Jalal Ale Ahmad Highway, P.O. Box 14115-143, Tehran, Iran
[2] Faculty of Engineering, Tarbiat Modares University, Jalal Ale Ahmad Highway, P.O. Box 14115-143, Tehran, Iran (**Corresponding author**)
[3] Department of Civil and Environmental Engineering, Tarbiat Modares University, Jalal Ale Ahmad Highway, P.O. Box 14115-397, Tehran, Iran

CC BY

Volume Particle Method (FVPM), Material Point Method [7], Multi Scale Finite Volume [8, 9], Hybrid Finite Element [10, 11] and many others, CFD technique has been widely adopted in a variety of engineering applications involving the fields of hydrodynamics and ocean engineering [7]. Generally, classical grid-based methods, such as the finite difference method (FDM) and finite element method (FEM), require expensive re-meshing algorithms or dynamic overlapping grids to avoid severe mesh distortions and associated errors. Recently, meshfree and particle methods have been applied in viscous incompressible flows with large deformation and free surface [7]. In order to model fluid and solid interactions, usually different methods are coupled together or one method integrates dissimilar forms of phase behavior. Here, the SPH and DEM are utilized to simulate water (as fluid) and structure (as solid), respectively. The highest purpose of performing numerical analyses is to replicate real-world experiments and problems, accordingly, many efforts have been being made. Some of the experiments and related simulations are listed in Table 1. From all of the mentioned experiments, only the dam break with an elastic gate and rapid flow scour tests are useful to monitor the solid-solid interactions; in other words, for the rest cases, solids can simply be treated as a boundary condition and the solid phase interactions (distribution of forces and movements in the solid) be ignored. Consequently, for coupled numerical analysis, it is more practical to consider an empirical scenario that considers not only fluid and fluid-solid interactions, but also solids nature.

Table 1. some experiments, alongside the methods verified by them

Experiments	Methods
Wedge entry test	SPH-SPH [12,13], SPH-DEM [14,15]
Cylinder entry and exit tests	SPH-SPH [13], Constrained Interpolation Profile (CIP) [16]
Landslide generated surge waves test	SPH-ISPH and SPH-DEM [17]
Rapid flow scour experiment	SPH-SPH and SPH-DEM [14]
Dam break with an elastic gate test	SPH-SPH [18,19], SPH-SPIM (Smoothed Point Interpolation Method) [20], SPH-DEM [17,3]

Discrete Element Method was introduced by Cundall for soil mechanics problems which later also aimed at rock mechanics problems [21, 22]. As a general rule discontinuum happens when some breakages happen in the continuum, therefore, a numerical method which is developed for discontinuous problems, must first be capable of solving continuous ones. Besides, there is a hidden advantage in using such methods in continuum computations, which is the procedure of

calibration becomes much simpler by omitting strength parameters. Considering this, in an effort, dynamic analysis of mountain movement was modeled in both PFC3D (DEM) and FLAC3D (FDM) [23], and in numerous attempts cantilever beams under point loads at their tips were modeled and compared with the analytical solution [3, 14, 24-27]. Generally, the DEM has three major shortcomings - excluding common limitations of the mesh-free methods: 1) constitutive laws are only applied at contacts. 2) results are highly influenced by damping forces 3) all parameters need to scale down to micromechanics level and to be calibrated.

The Smoothed Particle Hydrodynamics (SPH) was first introduced by Gingold and Monaghan [28] and L. B. Lucy [29] for solving astrophysics problems, and since then, the method is being used and undergone development, both in the formulation and boundary condition. In the following context, some of them which are the background knowledge of this research are referred. Campbell noticed the deficiency of kernel approximation in presence of boundary condition and stated the necessity of boundary treatment [30]. Monaghan used artificial viscosity in simulation of shock waves [31], employed the equation of state for hydrodynamics simulations, and used Lennard-Jones form as a penalty method to repulse fluid points from boundary [32]. Morris proposed another artificial viscosity formulation for low Reynolds number phenomenon [33]. In order to mitigate the SPH points' clustering, Monaghan added a term to the momentum equation to remedy tensile instability [34]. Crespo explained the basics and properties of dynamic boundary condition approach in which all boundary points' properties remain stationary exempt density and pressure which participate in continuity and state equations respectively [35]. Adami introduced ghost particle methods in which first boundary points' pressure is computed via interpolation, then density is calculated via the reverse of the state equation [36]. In general, the dynamic boundary approach is more stable and accurate than the ghost particles method [37]. Wu [3] employed a stationary boundary condition. Chiron introduced a new semi-analytical boundary method using wall treatment which has a precision close to ghost particles [38].

To couple the DEM and SPH, two general approaches exist [3]. In the first approach (which is based on the premise that each DEM particle is a completely separate object) the fluid and drag forces are calculated on DEM particles, then the sums of these forces are interpolated and used as reaction forces for SPH points [39-41]. In the second approach, the interactions are calculated employing the same formula used for fluid-fluid interaction with presumptive values for DEM particles' pressure and density [3, 18].

Regarding the single-phase SPH simulations, the method Wu [3] used for the boundary condition has not been tested in terms of reproducibility by other researchers. Also, they claimed that increasing smoothing lengths would benefit the results and proposed using dynamic smoothing length in future studies, whereas Jonsson [42] asserted that employing dynamic smoothing length had no significant effect on their results. Concerning two-phase SPH-DEM simulations, different coupling methods, have never been tested against one another.

The SPH and DEM (which are mesh-less methods) albeit their great capability in simulation of various problems, are not considered to be the primary choice for engineers, ascribable to their heavy computational costs. In these methods, each element's properties are calculated by considering how it is affected by any other element. As it is discussed later, these calculations can be reduced if only interactions within the domain of each DEM particle or SPH point are computed. There are mainly three ways for fulfilling this aim, using k-d tree, quad tree, or grid method algorithms. Here, the latter was used. Another approach to reduce run-times is to employ parallel computation. Nowadays NVIDIA Graphic Card Units (GPUs) are trending for parallel programming, best accessible and usable by the CUDA framework. On the contrary, one must bear in mind that parallel programming without precautions and proper changes in conventional

serial algorithms may result in longer run-times. Hence, in the current study, an optimized object-oriented algorithm is developed.

In the following, the DEM and SPH and their formulations are explored. How to use object-oriented parallel programming to better adapt the grid method explained. After that, for the purpose of validation, numerical tests such as beam deflection, dam break, dam break with an elastic gate (with three different approaches for coupling the SPH and DEM), and hydrostatic water column on an elastic plate are simulated and effects of variable smoothing length in the SPH and boundary conditions in the SPH and DEM is scrutinized.

2. Discrete element method

The role of the Discrete Element Method (DEM) in modeling solids is undeniable. The method is capable of modeling solids with the possibility of dispersions, detachments, and fractures. In this method, each one of the particles can be connected to one another through sets of springs if they are in each other's domain. In normal linear spring models, these springs only act if these particles are overlapping and otherwise no force would be produced, on the other hand, there are bonding models which concern the attachment and fracture of materials. Such models consider the gap between particles for tensile force calculations. With regard to the problems unrelated to the bonded particles it is advised to use Hertz-Mindlin model instead of the linear spring model [43].

Almost all DEM bonding methods are based on the contact and parallel bond models (for more information about the contact bond, interested readers can refer to reference [26]). The parallel bond model can be used alongside either the liner spring model or the contact bond model. Nevertheless, the first option is used more frequently, as it is employed here.

The total force applied to each particle in the DEM is:

$$\boldsymbol{F}^{total} = \Sigma \boldsymbol{F}^{CF} + \boldsymbol{F}^{b} + \boldsymbol{F}^{d} + \Sigma \boldsymbol{F}^{ext} \tag{1}$$

where $\boldsymbol{F}^{total}$ is the total force, $\boldsymbol{F}^{CF}$ is the contact force, $\boldsymbol{F}^{b}$ is the body force, $\boldsymbol{F}^{d}$ is the damping force and $\Sigma \boldsymbol{F}^{ext}$ is the sum of external forces (in association with the fluids, magnetic fields, applied loads, etc). In the DEM, the external and contact forces cause changes in linear and angular momentum of the DEM particles. This section is further continued to show how the contact, momentum, and damping forces are calculated and what is the basis of the parallel bond.

2.1. Linear spring model

The linear spring model consists of two types of springs; one lies on contact plane and the other one is in the direction of normal to contact plane. Therefore, the equations to calculate normal ($\boldsymbol{n}_i$) and shear ($\boldsymbol{t}_i$) vectors of each contact plane are (in 2D):

$$n_i = \frac{x_i^{[B]} - x_i^{[A]}}{d} \tag{2}$$

$$t_i = (-n_2, n_1) \tag{3}$$

where superscripts B and A denote the circular particles that are in contact, x_i is the reference coordinates, and d is the distance which can simply be calculated as:

$$d = |x_i^{[B]} - x_i^{[A]}| = \sqrt{(x_i^{[B]} - x_i^{[A]})(x_i^{[B]} - x_i^{[A]})} \quad (4)$$

For simplicity in this paper, we focus on an arbitrary particle A to explore the equations, and particle B resembles every arbitrary particle which is in contact with the particle A. Thus, every calculations must be repeated for each particle B that are in contact with the particle A.

The size of the overlap between the two particles is:

$$U^n = d - R^{[A]} - R^{[B]} \quad (5)$$

The normal spring model is only valid until U^n is negative (when the overlap is positive, no contact exists between the pair of particles, thus no force is transmitted).

In the DEM, particles are slightly overlapped to create bonds between them. If the direct approach to determine the overlap (equation 5) is used to compute the DEM forces, the initial forces in the simulation would be nonzero. Accordingly, using the direct approach to calculate the overlaps is impractical. Consequently, computing the overlap incrementally through the relative velocity is a better approach:

$$\Delta U^n = (\dot{x}_i^{[B]} - \dot{x}_i^{[A]}) n_i \Delta t \quad (6)$$

In this equation, ΔU^n is the incremental overlap, Δt is the elapsed time of each calculation cycle and $\dot{x}_i$ is the velocity. Note that, the value of shear displacement cannot be captured directly like equation 5 for the normal overlap, and can only be achieved incrementally using:

$$\Delta U^s = \boldsymbol{V}^s \Delta t \quad (7)$$

where $\boldsymbol{V}^s$ is the relative shear velocity and is computed by:

$$\boldsymbol{V}^s = (\dot{x}_i^{[B]} - \dot{x}_i^{[A]}) t_i - \boldsymbol{\omega}_3^{[B]} (R^{[B]} + \frac{U^n}{2}) - \boldsymbol{\omega}_3^{[A]} (R^{[A]} + \frac{U^n}{2}) \quad (8)$$

where $\boldsymbol{\omega}_3$ denotes the rotational velocity in z-direction.

Subsequent to the calculation of relative normal and shear displacements at the contact point, the contact forces can be updated using the normal and shear spring constants (k^n, k^s) using the following equations:

$$\Delta F^n = k^n \Delta U^n \quad (9)$$

$$\Delta F^s = k^s \Delta U^s \quad (10)$$

$$F^n \leftarrow F^n + \Delta F^n \quad (11)$$

$$F^s \leftarrow F^s - \Delta F^s \quad (12)$$

$$F^s = \min(F^s, \mu F^n) \quad (13)$$

$$F_i^{LSMCF[A,B]} = F^s t_i - F^n n_i \quad (14)$$

$$F_i^{CF[A]} \leftarrow F_i^{CF[A]} - F_i^{LSMCF[A,B]} \tag{15}$$

where ← denotes the assignment of its right-hand side value to its left-hand side variable, F^n is the normal force, F^s is the shear force, $F_i^{LSMCF[A,B]}$ is the linear spring model's force in the direction from particle A to particle B, and μ is the friction coefficient. It is also worth pointing out that equation 13 is used to enforce the slip condition.

Obviously, only shear force is responsible for producing angular momentum; Therefore, the moment caused by this contact force is:

$$M_3^{[A]} \leftarrow M_3^{[A]} - F^s(R^{[A]} + \frac{U^n}{2}) \tag{16}$$

where $M_3^{[A]}$ is the total moment of particle A. One should bear in mind that in equation 16, the moment vector is reduced to M_3 since here two-dimensional analyses are carried out.

2.2.Parallel Bond

In this perception of the bonded particles, each pair is connected to a beam-like element with the cross section area of A and moment of inertia of I, called cement. On this account, the cement elements are capable of transmitting and tolerating both axial forces and moments until a maximum value is reached. The model is defined by five bonding parameters: the normal stiffness $\bar{k}^n$, the shear stiffness $\bar{k}^s$, the normal strength $\bar{\sigma}_c$, the shear strength $\bar{\tau}_c$ and the bond radius $\bar{R}$. The bond radius is the radius of the cement and is equal to the mean or equivalent radius of two bonded particles multiplied by a constant ($\bar{R} = \alpha\frac{R^{[A]}+R^{[B]}}{2}$ or $\bar{R} = \alpha\frac{R^{[A]}R^{[B]}}{R^{[A]}+R^{[B]}}$). The forces $\bar{\boldsymbol{F}}$ and $\bar{\boldsymbol{M}}$ caused by the presence of a parallel bond are expressed incrementally by:

$$\bar{\boldsymbol{F}} = \bar{F}^s\boldsymbol{t} - \bar{F}^n\boldsymbol{n} \tag{17}$$

$$\bar{\boldsymbol{M}} = \bar{M}_3 \leftarrow \bar{M}_3 - \bar{k}^n I\Delta\theta_3 \tag{18}$$

where $\Delta\theta_3$ is the increment of rotation around the third axis ($\Delta\theta_3 = (\omega_3^{[B]} - \omega_3^{[A]})\Delta t$). $\bar{F}^n$ And $\bar{F}^s$ are computed through:

$$\bar{F}^n \leftarrow \bar{F}^n + \bar{k}^n A\Delta U^n \tag{19}$$

$$\bar{F}^s \leftarrow \bar{F}^s - \bar{k}^s A\Delta U^s \tag{20}$$

Now that the parallel bond's momentum and forces are calculated, they must be evaluated against the bond's normal and shear strength. These criteria are expressed by:

$$\frac{\bar{F}^n}{A} + \frac{|\bar{M}_3|\bar{R}}{I} < \bar{\sigma}_c \tag{21}$$

$$\frac{|\bar{F}^s|}{A} < \bar{\tau}_c \tag{22}$$

While these criteria are met, the bond between each bonded particle remains intact but as soon as violated the bond would disappear and the contact behavior would only be that of the linear spring model. Subsequently, if the bond is not broken, the forces and moments are added to the corresponding total values:

$$F_i^{CF[A]} \leftarrow F_i^{CF[A]} - \bar{F}_i \tag{23}$$

$$M_3^{[A]} \leftarrow M_3^{[A]} - \bar{F}^s(R^{[A]} + \frac{U^n}{2}) - \bar{M}_3 \tag{24}$$

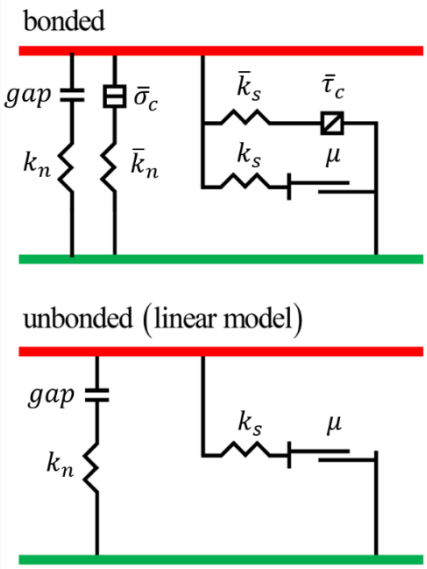


Figure 1. Bonded and unbonded contact laws of parallel bond model (adapted from reference [27]).

2.3.Damping

Since the DEM basically consists of a system of springs, it is safe to assume all interactions happen in the domain of elasticity unless some damping is introduced. The fact of the matter is that damping causes energy loss by reducing the total (unbalanced) forces, which consequently, leads to stability in the final stages of DEM simulations. Without damping, stability is not achievable, and as a result, the conclusions are occasionally profitable. There are different methods for introducing damping to a system such as the mass, viscous and local damping. The former is no longer used, since it leads to additional body forces, has a parameter related to the stiffness matrix, and all particles experiment the same damping [44]. The viscous damping is suitable for simulations involving free fall or impact between particles. This method is absolutely weak to make a simulation reach its final steady state. The other pitfall of this method is that viscous damping is not accustomed to the cement part of the parallel bond and only effects the linear spring model. In usual cases, parallel bond springs are much bigger in magnitude than those of linear model, thus the effect of this method of damping in the presence of parallel bond is unnoticeable. Currently, the last resort is to use the local damping. The local damping is generally not a good choice for problems engaging impacts, but is usable with a correct damping factor. For each particle, this form of damping is calculated via:

$$F_i^d = -\alpha |F_i^U| sign(v_i) \tag{25}$$

where α is the local damping constant, F_i^U is the unbalanced force (the total force before computing the damping) and $sign()$ is a function that returns the signature of an input variable (positive = +1, zero = 0 , negative = -1). Regularly, the constant is taken to be 0.7, yet in dynamic solutions, 0.157 is used, which corresponds to 5 percent of critical damping of a structure.

3. Smoothed Particle Hydrodynamics

The smoothed Particle Hydrodynamics (SPH), although capable of simulating all phases, is frequently employed to mimic fluid behavior. In this paper, likewise, this method is utilized to simulate water. In SPH, each point is an indicator of its surrounding properties, in a way that the closer we get to the center of a point on its domain, the more amplified the effect of its surrounding properties become. Considering an arbitrary point with its position vector x within its domain Ω, the general formulation of the SPH stems from the following equation:

$$f(x) = \int_{\Omega} f(\acute{\boldsymbol{x}}) \delta(\boldsymbol{x} - \acute{\boldsymbol{x}})\, d\Omega \tag{26}$$

where δ denotes the Dirac delta function, x is the position vector of every point in the domain of x and f is the property function. Having δ replaced by a smoothing function (W) and discretizing Ω, the basic form of the SPH is:

$$f(\boldsymbol{x}^{[A]}) = \sum_{B=1}^{n} f(\boldsymbol{x}^{[B]})\, W(\boldsymbol{x}^{[A]} - \boldsymbol{x}^{[B]}, h) \frac{m^{[B]}}{\rho^{[B]}} \tag{27}$$

where n is the total number of points in the domain, h is the smoothing length, m is the mass, and ρ is the density. In most researches, usually, Spline and Wendland smoothing function (kernels) are used. Here based on the recommendation [3], Wendland kernel is employed which has the following formulation (for two-dimensional):

$$W(q) = \begin{cases} \frac{7}{4\pi h^2}(1 - \frac{q}{2})^4 (2q+1) & 0 < q < 2 \\ 0 & q > 2 \end{cases} \tag{28}$$

where q is $^{d}/_{h}$ in which d is the distance. On many occasions, an approximation of divergence (for vector functions) and gradient (for scalar functions) of a certain property function is needed, which were derived from different perspectives based on the need and knowledge of SPH developers. Here, to apply divergence and gradient, the following equations are used, respectively.

$$\boldsymbol{\nabla}.\boldsymbol{f}(\boldsymbol{x}^{[A]}) = -\sum_{B=1}^{n} \frac{m^{[B]}}{\rho^{[B]}} (\boldsymbol{f}(\boldsymbol{x}^{[A]}) - \boldsymbol{f}(\boldsymbol{x}^{[B]})) . \boldsymbol{\nabla} W(\boldsymbol{x}^{[A]} - \boldsymbol{x}^{[B]}, h) \tag{29}$$

$$\nabla f(\boldsymbol{x}^{[A]}) = -\rho^{[A]} \sum_{B=1}^{n} m^{[B]} \left(\frac{f(\boldsymbol{x}^{[A]})}{(\rho^{[A]})^2} + \frac{f(\boldsymbol{x}^{[B]})}{(\rho^{[B]})^2}\right) \nabla W(\boldsymbol{x}^{[A]} - \boldsymbol{x}^{[B]}, h) \tag{30}$$

It is worth mentioning that equation 30 is also used for taking the divergence of a tensor.

Fundamental governing equations of fluid dynamics are the conservation of mass, momentum and energy which are the three basic physical laws of conservation. Usually, the third one is used when the change in energy is of high importance to a simulation's result (like shock problems), accordingly here is omitted.

3.1.Continuity equation

Based on the conservation of mass, the continuity equation is derived:

$$\frac{D\rho}{Dt} = -\rho \nabla . \boldsymbol{v} \tag{31}$$

where ρ is the density, $\frac{D}{Dt}$ is the material time derivative, $\nabla.$ is the divergence, and $\boldsymbol{v}$ is the velocity.

The continuity equation states that the rate of the mass imported to the system minus the rate of the mass exported from it, is equal to the accumulation of mass in that system.

One of the most significant approximations in SPH is the approximation of ρ, regarding its role in almost all SPH equations. Therefore, any miscalculation of ρ can result in an almost futile effort in the calculations of other approximations. On account of disproportionate densities in multi-phase simulations, an approximation like the below equation is needed, which has the benefit of using volume instead of density [36].

$$\frac{D\rho^{[A]}}{Dt} \simeq \rho^{[A]} \sum_{B=1}^{n} \frac{m^{[B]}}{\rho^{[B]}} (\boldsymbol{v}^{[A]} - \boldsymbol{v}^{[B]}) . \nabla W(\boldsymbol{x}^{[A]} - \boldsymbol{x}^{[B]}, h) \tag{32}$$

This equation is derived from substituting 29 in 31.

3.2.Momentum Equation

The equation of momentum is derived based on the equivalency of forces acting on an infinitesimal box in every local axial direction. This equation is expressed as:

$$\frac{Dv_i}{Dt} = -\frac{1}{\rho}\frac{\partial p}{\partial x_i} + \frac{1}{\rho}\frac{\partial \tau_{ij}}{\partial x_i} + F_i \tag{33}$$

where p is the pressure, τ_{ij} is the viscosity stress tensor, and F_i is the body force per mass. It is obvious that this equation consists of three terms, the gradient of pressure, divergence of viscosity stress tensor, and body force. The interpretation of the first term by the SPH is:

$$\left(-\frac{1}{\rho}\frac{\partial p}{\partial x_i}\right)^{[A]} = \sum_{B=1} m^{[B]} \left(\frac{p^{[A]}}{(\rho^{[A]})^2} + \frac{p^{[B]}}{(\rho^{[B]})^2}\right) \nabla W(\boldsymbol{x}^{[A]} - \boldsymbol{x}^{[B]}, h) \tag{34}$$

which is achieved by substituting equation 30 in pressure gradient term of equation 33.

As there is no way of knowing the pressure based on the continuity and momentum equations, a concept known as "the artificial compressibility" is used, inspired by the existence of the well-known direct correlation between density and pressure in fluids. One of the equations, founded on this concept is the "Tait equation":

$$p = \frac{100\rho_0 v_{max}^2}{\gamma}\left(\left(\frac{\rho}{\rho_0}\right)^{\gamma} - 1\right) \tag{35}$$

where ρ_0 is the reference density (for water $\rho_0 = 1000kg/m^3$), v_{max} is the maximum possible velocity in an environment, and γ is a constant usually taken to be seven [32, 45].

For computing the divergence of the viscosity tensor, generally, two approaches exist [45]: One) At first strain is calculated for each point, then, knowing that $\boldsymbol{\tau} = \mu\boldsymbol{\epsilon}$ (where μ is the dynamic viscosity and ϵ is the strain) and substituting equation 30, the divergence of $\boldsymbol{\tau}$ is figured out. Two) using a concept called artificial viscosity. Artificial viscosity used to be utilized only for inviscid dissipations (damping) in simulations, especially suitable for shock problems. Later this concept was further developed to involve the viscous dissipation even for low Reynolds numbers [33]. In this paper, the second approach was preferred considering its relatively higher run-time speed, and the below equation is used.

$$\left(\frac{1}{\rho}\frac{\partial \tau_{ij}}{\partial x_i}\right)^{[A]} = \sum_{B=1} m^{[B]}(\mu^{[A]} + \mu^{[B]})\left(\boldsymbol{v}^{[A]} - \boldsymbol{v}^{[B]}\right)\frac{(\boldsymbol{x}^{[A]} - \boldsymbol{x}^{[B]}).\boldsymbol{\nabla}W(\boldsymbol{x}^{[A]} - \boldsymbol{x}^{[B]}, h)}{\rho^{[A]}\rho^{[B]}(|\boldsymbol{x}^{[A]} - \boldsymbol{x}^{[B]}|^2 + 0.01h^2)} \tag{36}$$

The term $0.01h^2$ in equation 36 is only added to avoid singularity. Finally, the body force term, for common simulations, is equal to the standard gravity.

3.3. Corrections

Since we are dealing with a numerical method that involves probabilities and uncertainties, some corrections are needed to mitigate unnatural results. As mentioned before, the kernels are functions of distance and smoothing length, therefore, the smoothing length must be selected carefully. It is proposed to be chosen in a way that each point would have 20 other points in its influential domain for a two-dimensional analysis [45] (for Wendland kernel, radius of the influential domain is $2h$). A wiser decision is to make the smoothing length dynamically changeable during a simulation based on the variation of the density in an elapsed time step:

$$\frac{Dh}{Dt} = -\frac{1}{n_d}\frac{h}{\rho}\frac{D\rho}{Dt} \tag{37}$$

where n_d denotes the dimension number (here is 2). When the density of a point rises, it's smoothing length and influential domain decreases. Using equation 37 begs for special care; since each point has its own variable smoothing length, using kernel function for an interaction — twice — with two different smoothing lengths would violate the conservation rules. To clarify, in an extreme case, a point with a big h, acknowledges the presence of a point with a small h in its domain and involves it in its calculation but not reciprocally. To resolve this issue a mean

smoothing length must be considered ($h = \frac{h^{[A]}+h^{[B]}}{2}$) [45].

Another issue in the SPH simulations (called tensile instability) is that wherever the pressure is negative, the probability of points to clump together is strong. One way to avoid it, is by introducing an additional force term to equation 34 [34]:

$$\left(-\frac{1}{\rho}\frac{\partial p}{\partial x_i}\right)^{[A]} \leftarrow \left(-\frac{1}{\rho}\frac{\partial p}{\partial x_i}\right)^{[A]} + \sum_{B=1} \frac{m^{[B]}}{100}\left(\frac{\left|p^{[A]}\right|}{\rho^{[A]}} + \frac{\left|p^{[B]}\right|}{\rho^{[B]}}\right)\left(\frac{W(\boldsymbol{x}^{[A]} - \boldsymbol{x}^{[B]}, h)}{W(\Delta P, h)}\right)^4 \nabla W(\boldsymbol{x}^{[A]} - \boldsymbol{x}^{[B]}, h) \tag{38}$$

where ΔP is the points' initial spacing (resolution). Intending to diminish incoordination in movements of SPH points and bringing some uniformity into the shape of fluids, a term called XSPH correction is added to time integration methods (in this study, for both SPH and DEM, leapfrog time integration [45] is used). This term is [31]:

$$\frac{d\boldsymbol{r}^{[A]}}{dt} = \boldsymbol{v}^{[A]} - \epsilon \sum_{B=1}^{n} \frac{m^{[B]}}{\bar{\rho}^{[A,B]}} (\boldsymbol{v}^{[A]} - \boldsymbol{v}^{[B]}).\nabla W(\boldsymbol{x}^{[A]} - \boldsymbol{x}^{[B]}, h) \tag{39}$$

where $\bar{\rho}^{[A,B]}$ is the mean density value of point A and B, and ϵ is a number between 0 and 1, selected in relation to a simulation's conditions. Throughout the literature of the SPH there are many other corrections for different simulation problems, based on the results; the corrections explained in this section, seems to suffice here.

3.4. Boundary Condition

One of the most significant parts of each simulation, to be considered in advance is boundary conditions. Unfortunately, the SPH is notorious for handling such conditions in numerical ways (not from the scientific point of view). Currently, the closest step to scientifically treat boundary condition is the wall boundary method [38]. Bear in mind that equations 29 and 30 are applicable when the kernel is not truncated; Otherwise, treatments are needed [30, 38]. Essentially, when a point approaches a boundary, owing to lack of presence of the SPH points on the boundary side, no approximation of its surrounding would hold true. There are two methods to treat this problem. The first one is by bringing back the additional part of divergence or gradient formula, which was omitted based on the fact that the kernel smoothly reaches zero on its domain's boundary. Therefore, since the kernel in this condition doesn't reach zero, this omitted term must be considered. The second method is two fill the boundary with enough points to mitigate the problem.

On the ground that in the current research, the focus is on the point-particle interaction, the wall boundary method was not used. Instead, the stationary boundary condition method explained in section 5 is employed for the immobile SPH boundary points

4. GPU implementation

Conventional serial processing is the primary choice for many programmers due to its simplicity and existence of a vast number of methods, algorithms and guidelines that make this

sort of programming more manageable. On the other hand, users of such programs have to spend a devastating time before completing each task just for the sake of the programmers' convenience. This trade-off becomes unjust in numerical analyses especially for those developed based on the mesh-less technique. To balance it, programmers should adapt parallel programming techniques.

Currently, the best way of employing the power of parallel programming is offered by NVIDIA, which has been extending the capability and accessibility of their GPUs to be a handy tool for this purpose. These GPUs are accessible (programmable) via CUDA (Compute Unified Device Architecture) SDK (Software development kit) which is powered by the LLVM compiler. CUDA is constantly developed to support modern features of NVIDIA GPUs; however, object-oriented programming introduced in CUDA SDK version 3.0, still isn't properly adapted by programmers.

For this research, an object-oriented GPU based program called APAM (A Particle/Point-based Analyzer and Modeler) was developed. In this version of APAM (ver 1.3) the input data can be produced by any program as long as it is formatted (or reformatted) according to the custom format explained in its help documentation. After simulations are done the results of selected time-steps are exported to a series of CSV files, formatted to be used in post-processing software (here, ParaView is used). Other than the mentioned toolkits, the software is self-contained and does not include any additional libraries. Currently, we do not have a plan for the software distribution. When the time comes, it will be under the MIT license.

As explained in section 2, an interaction only exists if there is a connection or overlap between each pair of particles. In the same way (refer to section 3), the presence of a SPH point only affects the points that reside in its vicinity. It is not wise to test these criteria for every point or particle to see whether an interaction exists or not; instead, only neighbors should be scrutinized. To identify neighbors a nearest neighbor search algorithm must be adapted. Here, the method explained in reference [46] is altered and used.

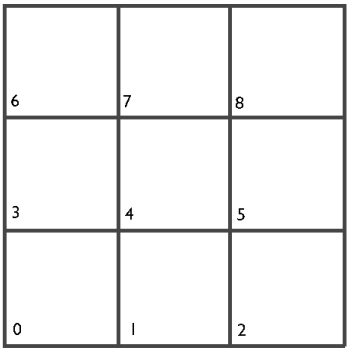


Figure 2. Partitioned space by cells. Numbers indicate cells' ID.

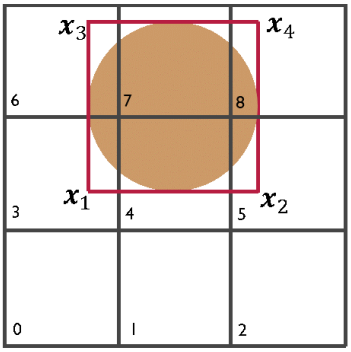


Figure 3. Boundary of each point or particle. For convenience in demonstration, colors are used for particles' or points' IDs, instead of numbers.

In this variation, first, an expected space is discretized into a series of cells. As an instance, Figure 2 shows a space divided into nine cells. Each cell contains properties of ID, an array of points' or particles' IDs, an array of connectors (which is discussed later), and numerators to save the position of the last input data to each mentioned arrays. Also, each particle or point, besides its properties (like mass, density, etc.), has an ID, an array of cells' IDs, and numerators with the

same application explained for a cell numerator.
Then, in each cycle of calculation the following procedure would be carried out:

1) Having the center and radius or influence radius for each particle or point, a square boundary can be calculated as it is shown in Figure 3. Only top right (x_4) and bottom left (x_1) points need to be computed and saved for each object.

2) In this step, each cell is allocated to the particles or points. To do so, knowing the bottom left and top right boundary coordinates for a particle or point (from the previous step), all the IDs of the cells that contain the space between these two coordinates are added to the particle's or point's array of cells' IDs. For further explanation, consider a space as depicted in Figure 4. After this step is done, the array of cells' IDs for each particle or point would be:

Red = {0,1,3,4} Blue = {1,2,4,5} Green = {7}

Notice that the data are stored in ascending order and no sorting algorithm is required.

3) Now the reverse of step 2 must be done. To put it another way, each particle or point is allocated to the cells. For the scenario depicted in Figure 4, the arrays of particles or points for each cell are:

Cell0 = {Red} Cell1 = {Red, Blue} Cell2 = {Blue}
Cell3 = {Red} Cell4 = {Red, Blue} Cell5 = {Blue}
Cell6 = {} Cell7 = {Green} Cell8 = {}

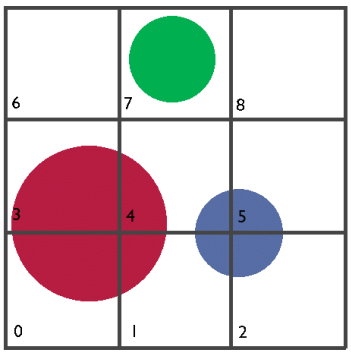


Figure 4. An example of points or particles positioned in space

Although for serialized programming, the mentioned allocations in the steps two and three can be done in one step, in parallel programming, doing so results in race condition. To avoid race condition, one must use atomic functions or redesign the algorithm. For this reason, in step three, there is a big sequential loop for all points and particles, wherein, for each of them a kernel (parallelly) would run that assigns the object to the related cells. Exempting the loop part of this step, all algorithms in APAM are run in parallel.

4) In this step, we create connectors. The connectors involve properties and methods based on how the relations for two particles or points or a pair of a particle and a point is defined, if they are connected. In order to create a connector, first, we scour each cell for the particles and points listed in its array. As an instance, look at Figure 4. In cell0 only one red object exists, thus no connection is possible, the same goes for Cell2, Cell3, Cell5, and Cell7, also for Cell6 and Cell8 which are empty. In Cell1 and Cell4, two objects (Red and Blue) exist simultaneously, and consequently, one of them must be selected valid for the creation of a connector, otherwise the presence of the multiple connectors for one pair, multiplies the result of the calculations.

Next, in order to select a valid cell, we go through the array of cells' IDs for each pair of objects. If the minimum of cells' IDs matches the current cell, this cell is selected as valid. For the

mentioned case, presume Cell1 is selected, and we want to check blue and red objects for connection. Then going through cells' IDs for these two, we find the minimum ID is 1. Therefore, Cell1 is selected valid. Clearly, this procedure doesn't validate Cell4 when it is selected. If a cell is valid for a pair and if they meet the connection criteria (overlap in the DEM or influence domain in the SPH), a connector is created.

5. Coupling SPH and DEM

Since DEM particles are representatives of solids, they can be treated as the boundary for the SPH points. There are numerous methods that treat boundary conditions by placing fixed SPH points on the boundary. These methods can be further developed into a context where SPH boundary points are replaced by DEM particles.

In this study, the stationary boundary condition method was used in all the simulations for immobile walls, and for movable boundary condition, all the methods expressed in the following (including the stationary boundary condition).

1) Stationary Boundary condition:

In this method, all the SPH boundary points' properties remain stationary throughout the simulations. When a non-boundary point approaches these boundary points, only equations 32, 34 and 36 is calculated for these interactions and the results only affects non-boundary points.

2) Pressure gradient:

Taking the pressure term in equation 33 into consideration and approximate it by the SPH method, the following term is achieved:

$$\boldsymbol{F}^{[F,S]} = -\frac{m^{[F]}m^{[S]}}{\rho^{[F]}\rho^{[S]}} P^{[F]} \boldsymbol{\nabla} W(\boldsymbol{x}^{[F]} - \boldsymbol{x}^{[S]}, h) \tag{40}$$

where $\boldsymbol{F}^{[F,S]}$ is the force applied to fluid from a solid particle. The force applied from the fluid to the solid is the same in magnitude but in reverse direction.

3) Pressure approximation: Simply, by substituting pressure into equation 27, the SPH approximation of pressure for each DEM particle is:

$$P^{[S]} = \sum_{F=1}^{n} P^{[F]}\, W(\boldsymbol{x}^{[S]} - \boldsymbol{x}^{[F]}, h) \frac{m^{[F]}}{\rho^{[F]}} \tag{41}$$

Now, having the DEM particles' pressure calculated, their density is estimated via the reverse of equation 35. The force between the SPH points and DEM particles is achieved by employing equation 34.

6. Numerical tests

In this section, the reliability of APAM code is tested and the expressed methods are validated by a few examples.

6.1.Beam deflection

To validate a DEM code, typically, a beam under a single load is simulated. Since it requires a minimum amount of calculations, the results are relatively fast to achieve. Here, to verify APAM, almost the same example that Itasca uses for validation of DEM is used [27]. Deflection of a

cylindrical beam with a radius of 8 in, length of 200 in, shear modulus of 3759.4 $kips/in^2$ and elastic modulus of 10000 $kips/in^2$, under 1 $kips$ load is -0.082893 in. To model this example using the parallel bond, 11 particles with a radius of 10 in and the parameters listed in Table 2 were used. Bear in mind that in this test, particles' shape is considered to be spherical (instead of cylindrical) in both PFC2D and APAM.

Table 2. Beam deflection parameters for parallel bond validation

Parameter	Value	Parameter	Value
$k^n = k^s$	$2.0106 \times 10^5 \ \frac{kips}{in}$	μ	0
$\bar{k}^n$	$500 \ \frac{kips}{in^3}$	$\bar{R}$	4 in
$\bar{k}^s$	$188 \ \frac{kips}{in^3}$	Δt	3.154 s

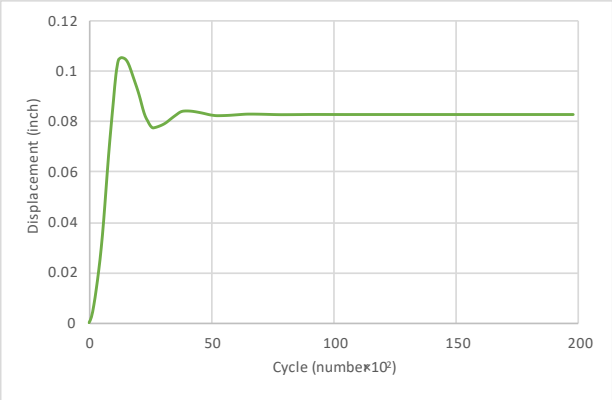


Figure 5. Plot of convergence study for the beam deflection

After 19800 cycles, 0.082948 in was reported from APAM (see Figure 5) for the beam's deflection, which is within the error of 0.1 percent.

6.2.Dam break

This experiment simply consisted of a water column enclosed in a tank by its walls and a barrier. Then, the barrier was instantly removed, and photos of water collapse and flow were taken in time intervals of 0.2s. To verify the SPH code, this simulation was carried out with the following properties and parameters, which is similar to what reported in [3].

Table 3. Dam break parameters for SPH validation

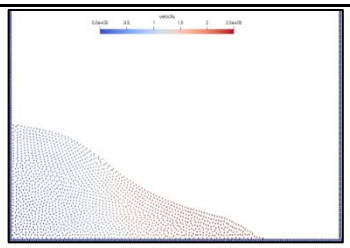
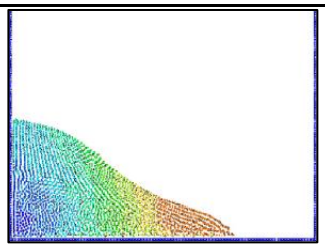
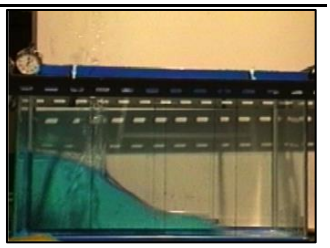
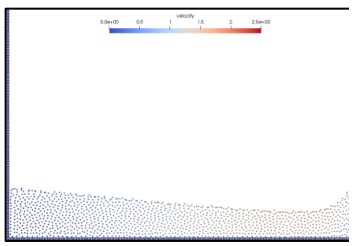
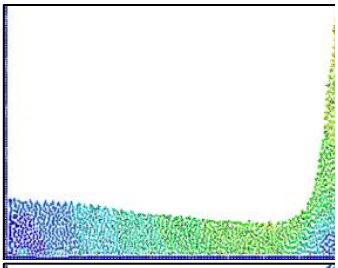
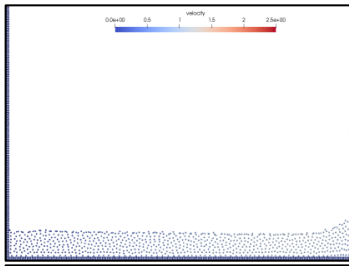
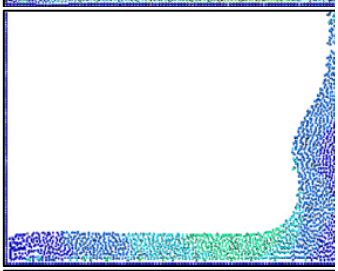
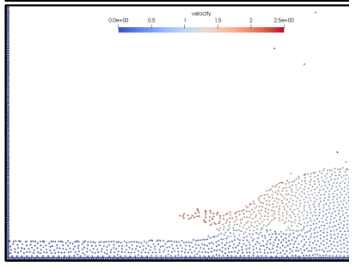
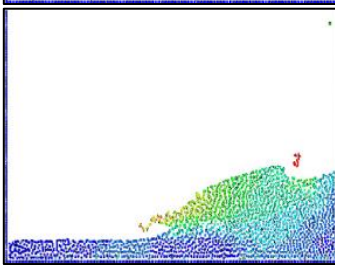
Parameter	Value
Boundary points' spacing	0.0025 m
Fluid points' spacing	0.005 m
Initial smoothing length	0.00625 m
Water's density	1000 Kg/m^3
Water's viscosity	$8.9 * 10^{-4}$ Pa.s
Time steps' interval	$4 * 10^{-6}$ s
Number of time steps	250000

The differences between this study and paper [3] are that here, the anti-clump term is not applied in fluid-boundary interactions (only used in fluid-fluid interactions), moreover, here, we utilized dynamic smoothing length. As can be seen in Table 4, these differences led to a boost in the results. Until 0.6s, a close resemblance exists between the two studies and the experiment. After that, especially in the presentations of the tunnel wave at 0.8s and the turbulence and voids at 1.0s, this study has an edge.

6.3.Dam break with an elastic gate

In this experiment, the procedure is similar to what is elucidated in section 6.2; the difference is that between the barrier and the water a rubber gate (fixed at its top) was installed and when the barrier was removed, the movement of water level behind the gate and displacement of the gate's bottom end was monitored against a graph paper. Parameters used to simulate this experiment are listed in Table 5.

Table 4. Dam break simulation and comparison for the SPH validation

Time	Current Work	SPH [3]	Experiment [3]
0.2 s			
0.4 s			
0.6 s			
0.8 s			

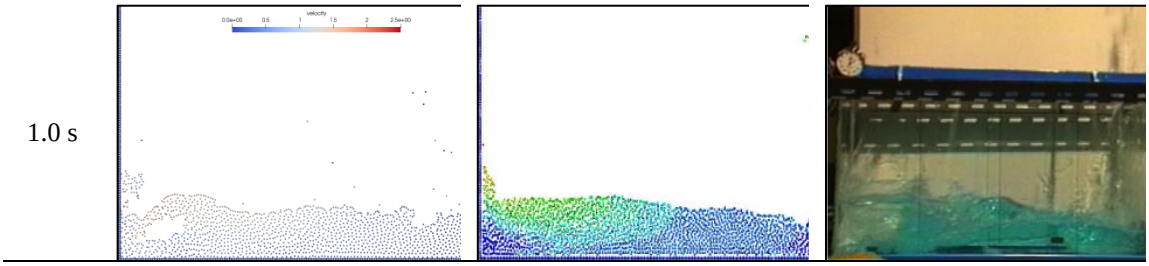


Table 5. Parameters and values used in the dam break with an elastic gate test

Parameter	Value
Boundary points' spacing	0.00125 m
Fluid points' spacing	0.00175 m
Initial smoothing length	0.0021875 m
Water's density	1000 Kg/m^3
Water's viscosity	8.9 * 10^{-4} Pa.s
Elasticity of the gate	10-12 MPa
Poisson's ratio of the gate	0.33-0.4
Diameter of DEM particles	0.00125 m
Time steps' interval	4 * 10^{-6} s
Number of time steps	100000

Before modeling this experiment, the gate itself was modeled several times as a cantilever beam with the aim of calibration. Parallel bond parameters can be calculated via:

$$\bar{k}^n = \frac{E}{R^{[A]} + R^{[B]}}, \quad \bar{k}^s = \frac{G}{R^{[A]} + R^{[B]}} \tag{42}$$

$$k^n = \frac{E(2\bar{R})}{R^{[A]} + R^{[B]}}, \quad k^s = \frac{G(2\bar{R})}{R^{[A]} + R^{[B]}} \tag{43}$$

where G is the shear modulus and $\bar{R}$ is the parallel bond radius. There are two procedures for calibration, the first one is to reduce the bond radius, and the second one is to change E and G until a reasonable error, is reached. For simulations in this section, the former is used and the latter is explained and employed in section 6.4.

To simulate this experiment correctly, several methods were used and a few attempts were carried out. The detailed explanation of the SPH-DEM coupling methods, employed in the following, was given in section 5.

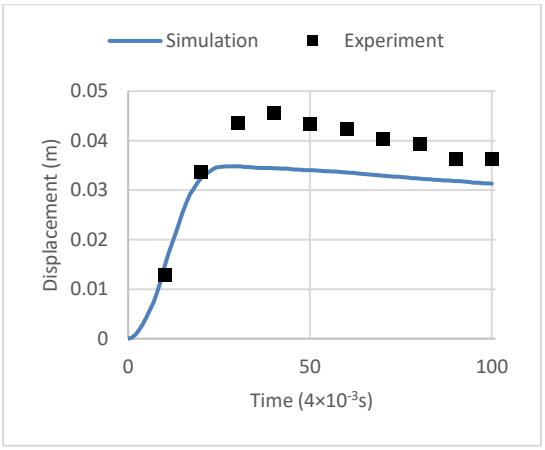
6.3.1. Stationary boundary condition

In the first attempt, the elastic modulus of 12 MPa, Poisson's ratio of 0.33, and local damping constant of 0.157 was considered for the rubber gate. Figure 6 shows the results. The horizontal and vertical displacements of the free end of the beam did not reach the experiment's peak values, and after reaching their peaks, decreased with very small slopes.

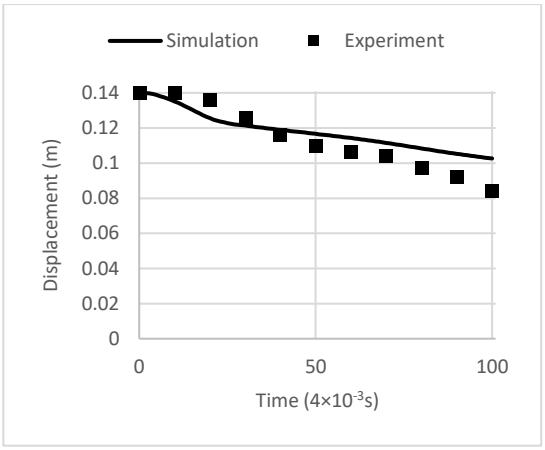
In the second attempt, the viscosity and XSPH were neglected, moreover, constant damping was set to 0.0134. The results of this try are depicted in Figure 7. This time, the vertical and

horizontal displacement of the free end of the beam reached higher peak values, however, their descending trends, started with a much bigger slope. On the other hand, the achieved water level shows a close agreement with the experiment. The results are similar to what reported in reference [47] and close to work of Liu [48].

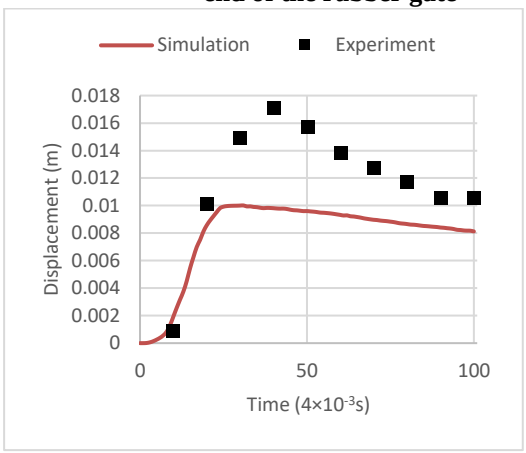
In the third attempt, likewise all the remaining methods in subsection 6.3, the XSPH and viscosity are considered, and the elastic modulus of 10 MPa, Poisson's ratio of 0.4, local damping constant of 0.157 were set for the rubber gate; another difference is that the DEM particles at the top end are not fully fixed. As can be seen from Figure 8, the middle particles are fixed and the side particles are left free.



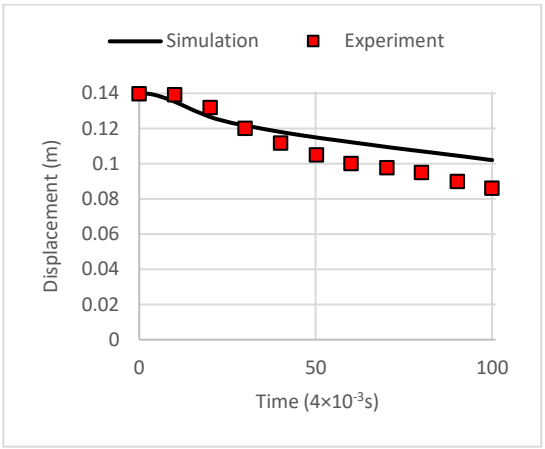
a) horizontal displacement of the free end of the rubber gate



c) water level just behind the gate

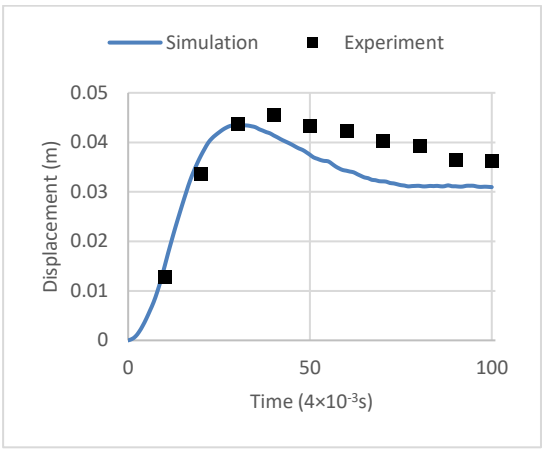


b) vertical displacement of the free end of the rubber gate

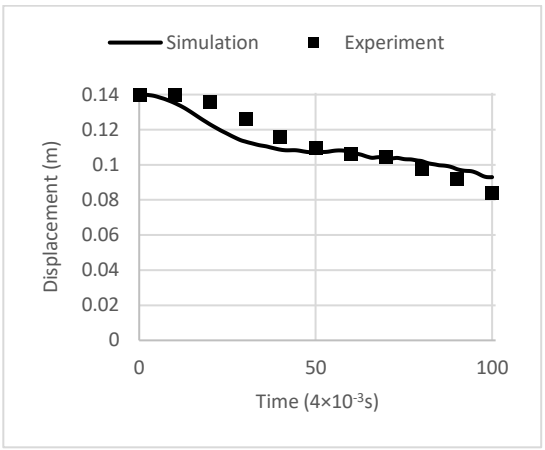


d) water level 5cm behind the gate

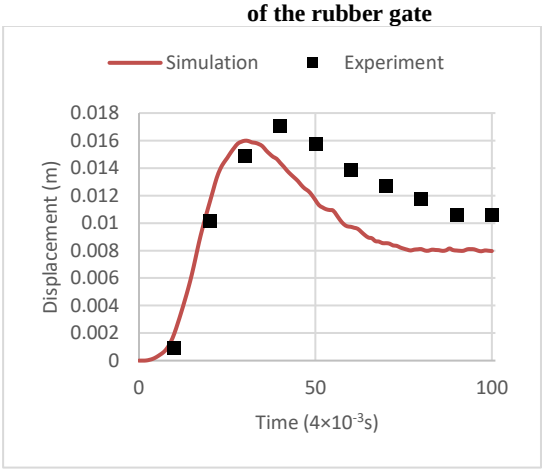
Figure 6. Plots of the stationary boundary condition method (first attempt)



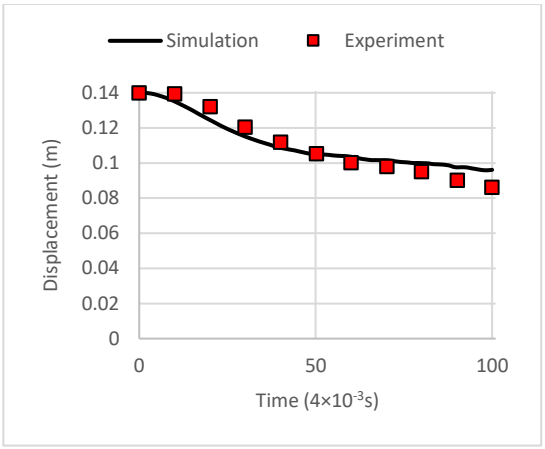
a) horizontal displacement of the free end of the rubber gate



c) water level just behind the gate

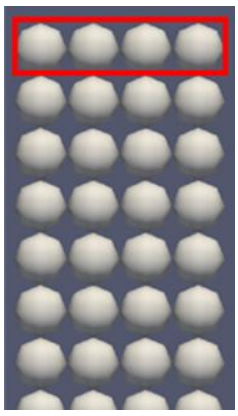


b) vertical displacement of the free end of the rubber gate

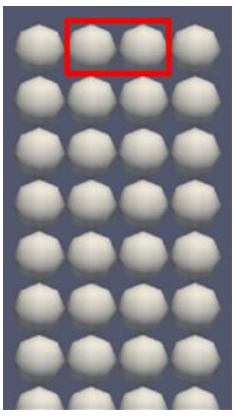


d) water level 5cm behind the gate

Figure 7. Plots of the stationary boundary condition method (second attempt)



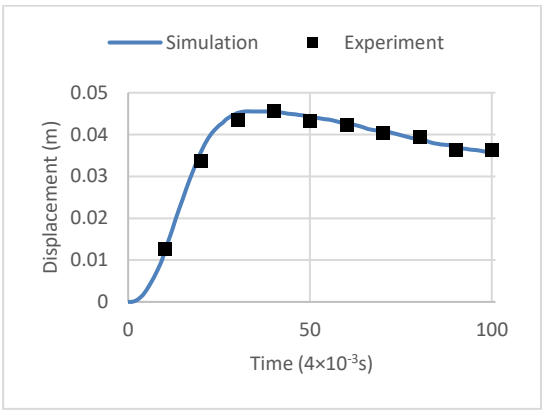
a) DEM boundary in previous attempts



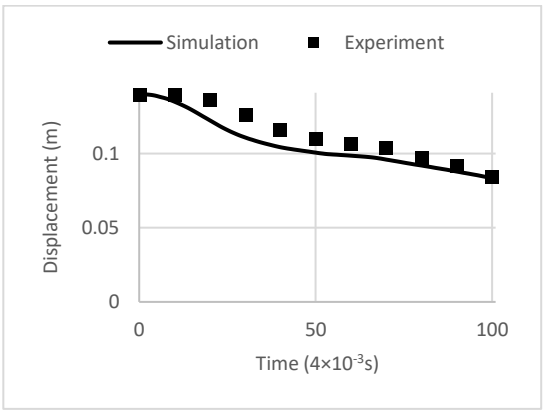
a) DEM boundary in current and sub-sequential simulations in subsection 6.3

Figure 8. DEM particles, particles enclosed by the red box are fixed and others are free

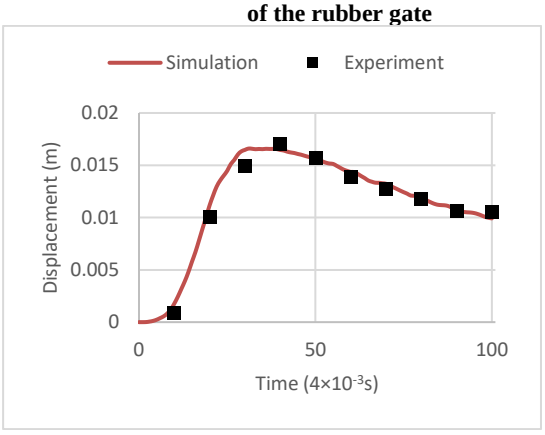
The reason for considering such DEM boundary condition is based on the premise that in reality there is no rigid boundary (especially for low elasticity materials like rubber) and by freeing the side particles, a semi-rigid boundary can be achieved.



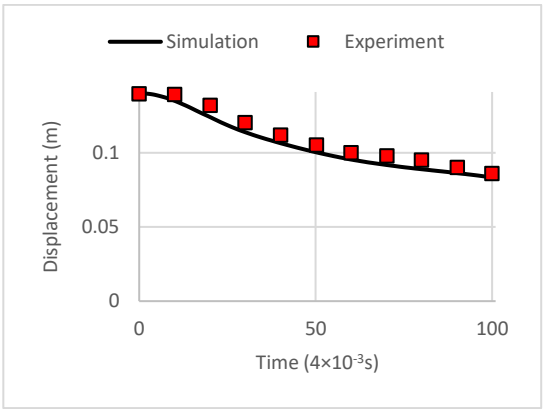
a) horizontal displacement of the free end of the rubber gate



c) water level just behind the gate

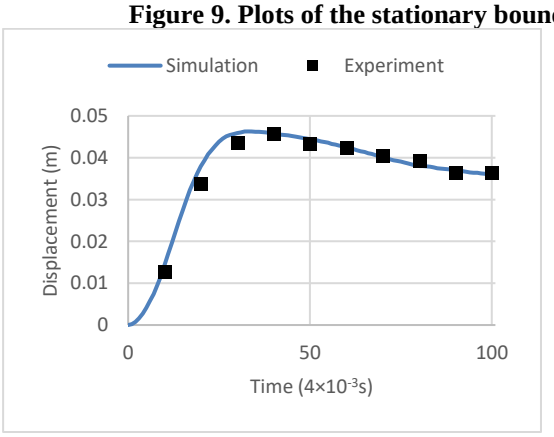


b) vertical displacement of the free end of the rubber gate

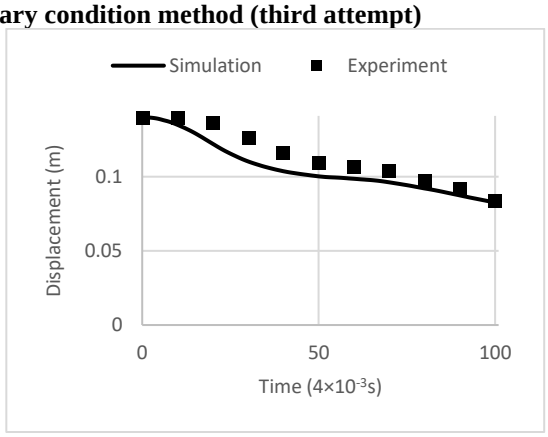


d) water level 5cm behind the gate

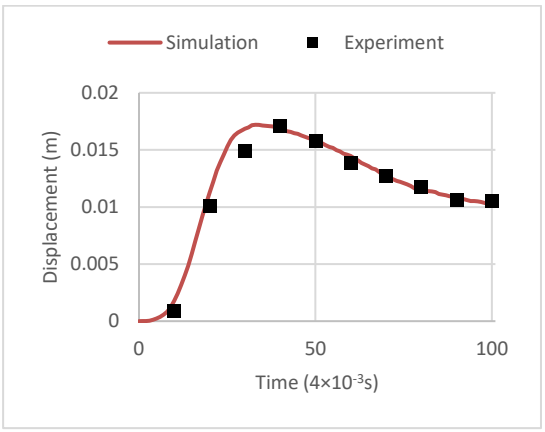
Figure 9. Plots of the stationary boundary condition method (third attempt)



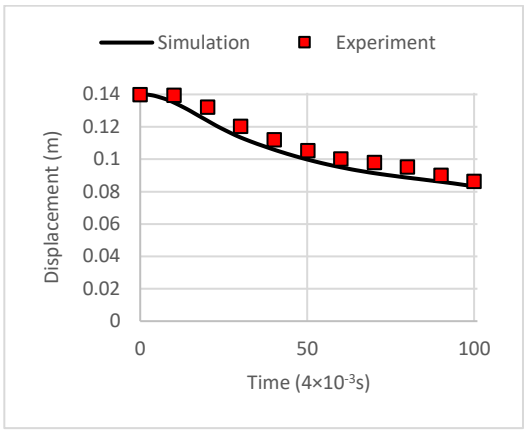
a) horizontal displacement of the free end of the rubber gate



c) water level just behind the gate

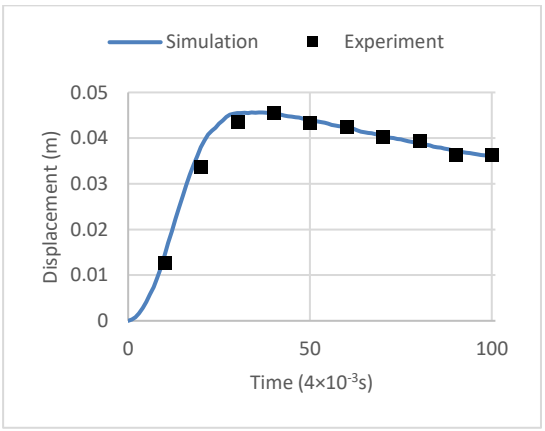


b) vertical displacement of the free end of the rubber gate

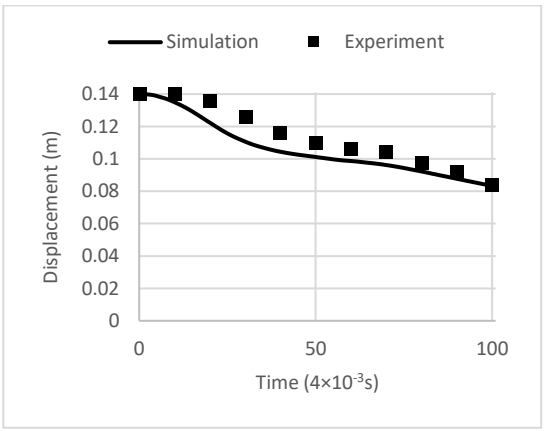


d) water level 5cm behind the gate

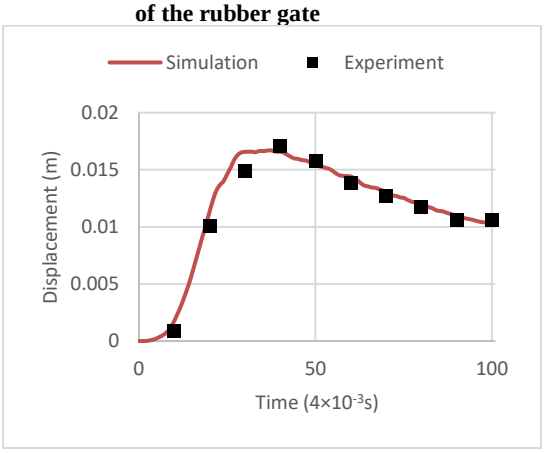
Figure 10. Plots of the pressure gradient method



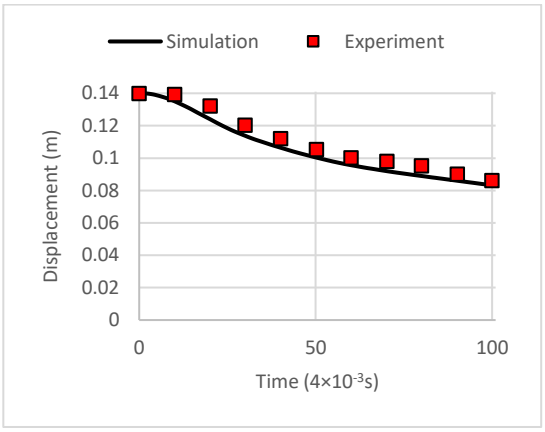
a) horizontal displacement of the free end of the rubber gate



c) water level just behind the gate



b) vertical displacement of the free end of the rubber gate



d) water level 5cm behind the gate

Figure 11. Plots of the pressure approximation method

As can be seen in Figure 9, in this attempt, although the vertical and horizontal displacements of the free end of the gate have reached their peak values faster than the experiment, their trends match up well with it. Now that a reasonable result was achieved, other methods were tested with the same configuration.

6.3.2. Pressure gradient and approximation methods

The results of the pressure gradient and pressure approximation methods are illustrated in Figures 10 and 11, respectively. In these three figures (Figures 9, 10 and 11), the results are shown to be very close to one another; nevertheless, the pressure gradient method is the least noisy among them. In Table 6, the shots of the experiment alongside the results from the pressure gradient method are presented, where the similarity in the shape of the water behind the gate, with that of physical test can be vividly observed.

The modifications used in this section are not unknown to the literature. In the work of Wu [3], the hexagonal packing was done in a manner that caused a semi-rigid boundary condition and in the study of Tang [14] the rubber beam was considered more porous by reducing the parallel bond radius.

6.3.3. Elastic plate under a water column in the hydrostatic condition

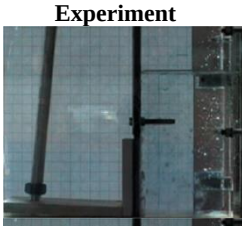
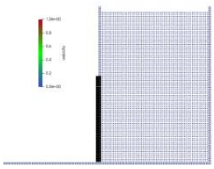
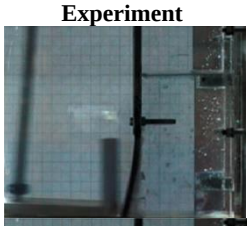
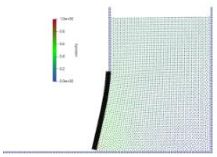
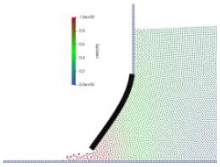
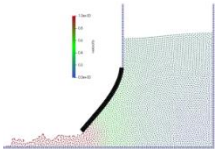
In this section, analytical solutions for a cantilever beam under a point load, and midpoint displacement of an elastic plate under a water column in the hydrostatic condition are used for validation. Vertical displacement of the plate midpoint under such spread loading is [49]:

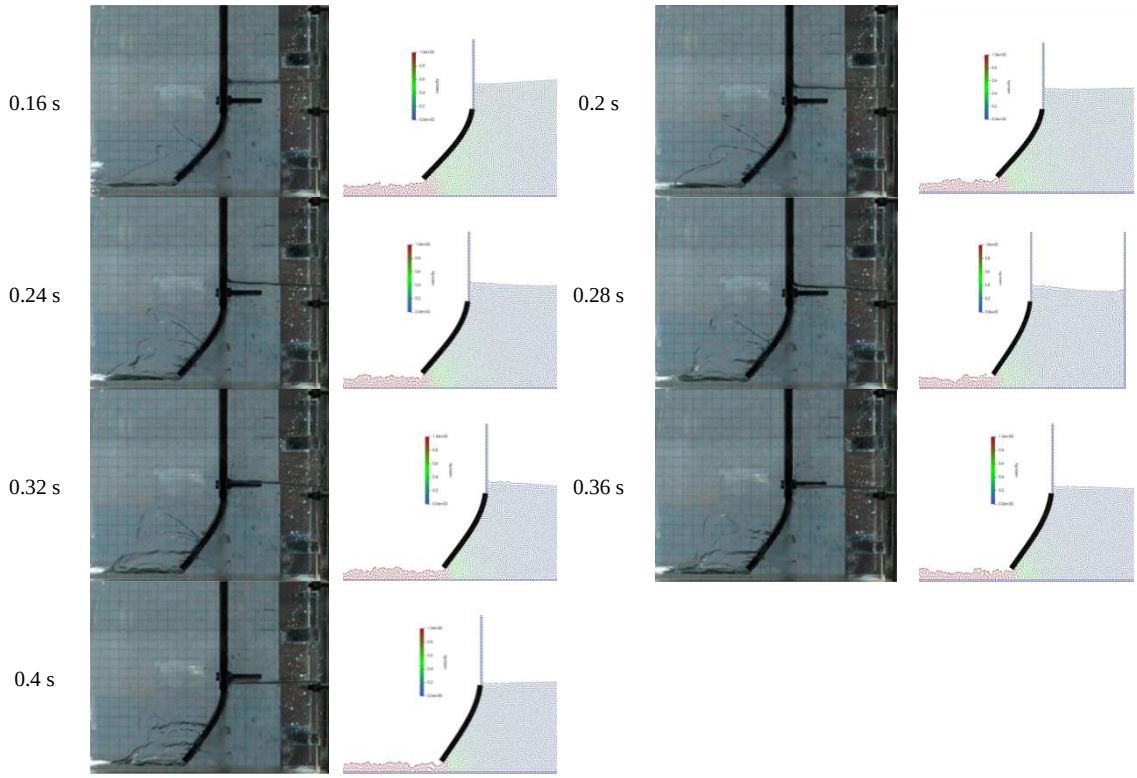
$$\omega = 0.0026g\frac{(\rho_{water}H + \rho_{plate})eL^4}{D} \tag{44}$$

And

$$D = \frac{Ee^3}{12(1-\nu^2)} \tag{45}$$

Table 6. Dam break with an elastic gate, the simulation's pictures are taken from the application of pressure approximation method

Time	Experiment	Current Work	Time	Experiment	Current Work
0.0 s			0.04 s		
0.08 s			0.12 s		



where H is the water height, e is the plate height, L is the plate length, and ν is the Poisson's ratio. Here, the pressure gradient method was used to couple the SPH and DEM. Elastic modulus was calculated from hook's law in the theory of linear elasticity [50]:

$$E \leftarrow \frac{E(1-\nu)}{(1+\nu)(1-2\nu)} \tag{45}$$

Then, this E was substituted in equations 42 and 43, and the bond radii were equal to the particles' radii. Also, the ratio of normal to shear springs (after the calibration procedure) was selected to be 2 (i.e. $k_s = 0.5k_n$ and $\bar{k}^s = 0.5\bar{k}^n$).

For a cantilever beam with a height of 5mm and length of 7.9375 cm, the tip displacement is 1.6 mm, when the applied force is 1N. To simulate it, first, we discretized this beam as shown in Figure 12. Then, by applying 1 N load at the center of tip particles and cycling until reaching equilibrium (Figure 13), tip displacement was achieved as 1.536 mm, which shows 4 percent error.



Figure 12. Discretized beam

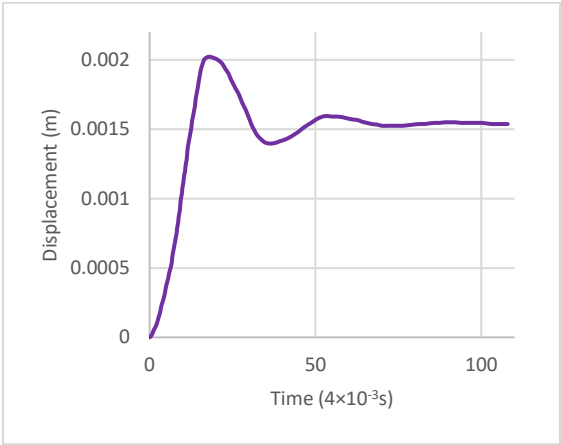


Figure 13. Tip displacement of a beam with length and height of 7.9375cm and 5mm, respectively, under 1N applied load

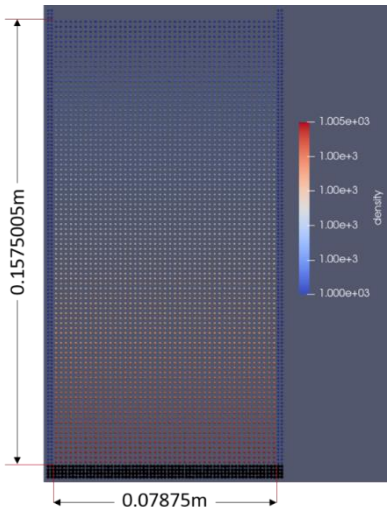


Figure 14. Discretized static tank

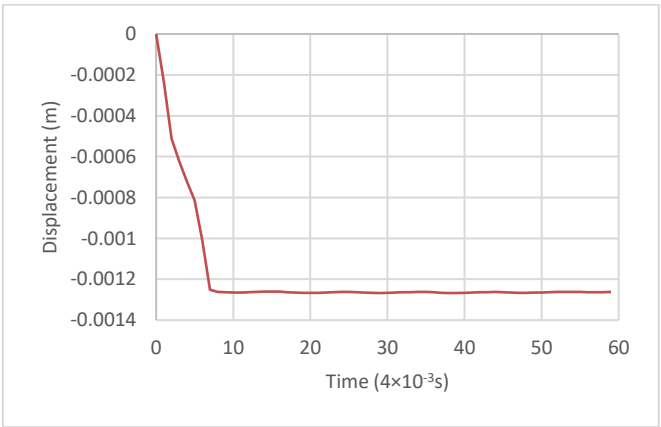


Figure 15. The beam's midpoint displacement

Then, we put the same beam with a nearly exact configuration under a hydrostatic water column. As depicted in Figure 14, the height and width of the water column are 0.1575005 m and 0.07875 m, respectively and the width of the beam is 5 mm. Furthermore, the density was taken to be 1000 kg/m^3 for water and 1100 kg/m^3 for the beam, moreover, the Poisson's ratio of 0.4 and 9.81 m/s^2 for the gravity was considered.

Analytically, displacement of the plate's midpoint is 0.0012895 m and numerically, it reached 0.001263 m which is only 2 percent error (Figure 15).

7. Conclusions

In this paper a combined SPH-DEM numerical modelling approach was proposed and validated for simulation of fluid-structure interaction problems. three methods of coupling the SPH and DEM (stationary boundary condition, pressure gradient, and pressure approximation), were explored, and acceptable results were achieved from validation of the code developed in this research and experiment, in all three of them. However, among these methods, there exists a barely noticeable difference in the maximum of displacements of the free end of the beam in the dam break with an elastic gate test and how this maximum is reached. Moreover, it was shown that the way boundary condition is regarded for the fixed end in the DEM, can be tremendously effective on the results and here, a semi-rigid boundary condition for the DEM is developed, and it is hoped to be investigated further to find better ways to simulate it. To model these mesh-less methods, an enhanced neighbor search algorithm with fewer locks was developed for GPU based computing. In the SPH single-phase simulation of the dam break experiment, the effect of dynamic smoothing length and boundary condition was seen so impressive that single-handedly improved the resultant replication (especially in the simulation of wave tunnel at 0.8s and shape of final turbulence at 1.0s). Finally, the pressure gradient method was tested against two analytical solutions of cantilever beam and hydrostatic water column on an elastic plate, simultaneously, with the errors of 4 and 2 percent, respectively.

References

1. Krevor SCM, Pini R, Li B, Benson SM. Capillary heterogeneity trapping of CO2 in a sandstone rock at reservoir conditions. *Geophysical Research Letters* 2011; 38(15). doi: 10.1029/2011gl048239.
2. Fakhimi A, Lanari M. DEM–SPH simulation of rock blasting. *Computers and Geotechnics* 2014; 55: 158-164. doi: https://doi.org/10.1016/j.compgeo.2013.08.008.
3. Wu K, Yang D, Wright N. A coupled SPH-DEM model for fluid-structure interaction problems with free-surface flow and structural failure. *Computers and Structures* 2016; 177: 141-161. doi: https://doi.org/10.1016/j.compstruc.2016.08.012.
4. Liang Q. Flood simulation using a well-balanced shallow flow model. *Journal of hydraulic engineering* 2010; 136(9): 669-675.
5. Gong Gb, Zha Xx. DEM simulation of liquefaction for cohesionless media at grain scale. *Journal of Central South University* 2012; 19(9): 2643-2649. doi: 10.1007/s11771-012-1322-9.
6. Müller M, Schirm S, Teschner M. Interactive blood simulation for virtual surgery based on smoothed particle hydrodynamics. *Technology and Health Care* 2004; 12(1): 25-31.
7. Liu Mb, Huang C, Zhang Am. Modelling incompressible flows and fluid-structure interaction problems with smoothed particle hydrodynamics: Briefing on the 2017 SPHERIC Beijing

International Workshop. *Journal of Hydrodynamics 2018; 30(1): 34-37. doi: 10.1007/s42241-018-0003-z.*

8. Sadrnejad S, Ghasemzadeh H, Taheri E. Multiscale multiphysic mixed geomechanical model in deformable porous media. *International Journal for Multiscale Computational Engineering* 2014; 12(6).
9. Taheri E, Sadrnejad S, Ghasemzadeh H. Multiscale geomechanical model for a deformable oil reservoir with surrounding rock effects. *International journal for multiscale computational engineering* 2015; 13(6).
10. Ghoreishian Amiri SA, Sadrnejad SA, Ghasemzadeh H. A hybrid numerical model for multiphase fluid flow in a deformable porous medium. *Applied Mathematical Modelling* 2017; 45: 881-899. doi: https://doi.org/10.1016/j.apm.2017.01.042.
11. Ghoreishian Amiri SA, Taheri E, Lavasan AA. A hybrid finite element model for non-isothermal two-phase flow in deformable porous media. *Computers and Geotechnics* 2021; 135: 104199. doi: https://doi.org/10.1016/j.compgeo.2021.104199.
12. Oger G, Doring M, Alessandrini B, Ferrant P. Twodimensional SPH simulations of wedge water entries. *Journal of Computational Physics* 2006; 213(2): 803-822. doi: https://doi.org/10.1016/j.jcp.2005.09.004.
13. Vandamme J, Zou Q, Reeve DE. Modeling Floating Object Entry and Exit Using Smoothed Particle Hydrodynamics. *Journal of Waterway, Port, Coastal, and Ocean Engineering* 2011; 137(5): 213-224. doi:10.1061/(ASCE)WW.1943-5460.0000086.
14. Tang Y, Jiang Q, Zhou C. A Lagrangian-based SPH-DEM model for fluid–solid interaction with free surface flow in two dimensions. *Applied Mathematical Modelling* 2018; 62: 436-460. doi: https://doi.org/10.1016/j.apm.2018.06.013.
15. Ren B, Jin Z, Gao R,Wang Yx, Xu Zl. SPH-DEM modeling of the hydraulic stability of 2D blocks on a slope. *Journal of Waterway, Port, Coastal, and Ocean Engineering* 2013; 140(6): 04014022.
16. Zhu X, Faltinsen OM, Hu C.Water entry and exit of a horizontal circular cylinder. *Journal of Offshore Mechanics and Arctic Engineering* 2007; 129(4): 253–264.
17. Tan H, Chen S. A hybrid DEM-SPH model for deformable landslide and its generated surge waves. *Advances in Water Resources* 2017; 108: 256-276. doi: https://doi.org/10.1016/j.advwatres.2017.07.023.
18. Antoci C, Gallati M, Sibilla S. Numerical simulation of fluid–structure interaction by SPH. *Computers and Structures* 2007; 85(11): 879-890. doi: https://doi.org/10.1016/j.compstruc.2007.01.002.
19. Liu Mb, Shao Jr, Li Hq. Numerical simulation of hydroelastic problems with smoothed particle hydrodynamics method. *Journal of Hydrodynamics* 2013; 25(5): 673-682. doi: 10.1016/S1001-6058(13)60412-6.
20. Zhang G, Wang S, Sui Z, Sun L, Zhang Z, Zong Z. Coupling of SPH with smoothed point interpolation method for violent fluid-structure interaction problems. *Engineering Analysis with Boundary Elements* 2019; 103: 1-10. doi: https://doi.org/10.1016/j.enganabound.2019.02.010.

21. Cundall PA, Strack ODL. A discrete numerical model for granular assemblies. *Géotechnique* 1979; 29(1): 47-65. doi: 10.1680/geot.1979.29.1.47.
22. Potyondy DO, Cundall PA. A bonded-particle model for rock. *International Journal of Rock Mechanics and Mining Sciences* 2004; 41(8): 1329-1364. doi: https://doi.org/10.1016/j.ijrmms.2004.09.011.
23. Bazgard A, Cundall PA, Davies TR. Dynamic analysis of mountain response using PFC3D and FLAC3D. In: ; 2011.
24. Tavarez FA, Plesha ME. Discrete element method for modelling solid and particulate materials. *International journal for numerical methods in engineering* 2007; 70(4): 379-404.
25. André D, Iordanoff I, Charles Jl, Néauport J. Discrete element method to simulate continuous material by using the cohesive beam model. *Computer Methods in Applied Mechanics and Engineering* 2012; 213-216: 113-125. doi: https://doi.org/10.1016/j.cma.2011.12.002.
26. Fakhimi A. A hybrid discrete–finite element model for numerical simulation of geomaterials. *Computers and Geotechnics* 2009; 36(3): 386-395. doi: https://doi.org/10.1016/j.compgeo.2008.05.004.
27. Itasca Consulting Group I. PFC 6.0 documentation. 2018.
28. Gingold RA, Monaghan JJ. Smoothed particle hydrodynamics: theory and application to non-spherical stars. *Monthly notices of the royal astronomical society* 1977; 181(3): 375-389.
29. Lucy LB. A numerical approach to the testing of the fission hypothesis. *The astronomical journal* 1977; 82: 1013-1024.
30. Campbell PM. Some new algorithms for boundary value problems in smooth particle hydrodynamics. report, MISSION RESEARCH CORP ALBUQUERQUE NM; 1989.
31. Monaghan J. On the problem of penetration in particle methods. *Journal of Computational physics* 1989; 82: 1-15.
32. Monaghan JJ. Simulating Free Surface Flows with SPH. *Journal of Computational Physics* 1994; 110(2): 399-406. doi: https://doi.org/10.1006/jcph.1994.1034.
33. Morris JP, Fox PJ, Zhu Y. Modeling Low Reynolds Number Incompressible Flows Using SPH. *Journal of Computational Physics* 1997; 136(1): 214-226. doi: https://doi.org/10.1006/jcph.1997.5776.
34. Monaghan JJ. SPH without a Tensile Instability. *Journal of Computational Physics* 2000; 159(2): 290-311. doi: https://doi.org/10.1006/jcph.2000.6439.
35. Crespo A, Gómez-Gesteira M, Dalrymple RA. Boundary conditions generated by dynamic particles in SPH methods. 2007.
36. Adami S, Hu XY, Adams NA. A generalized wall boundary condition for smoothed particle hydrodynamics. *Journal of Computational Physics* 2012; 231(21): 7057-7075. doi: https://doi.org/10.1016/j.jcp.2012.05.005.
37. Liu S, Nistor I, Mohammadian M. Evaluation of the Solid Boundary Treatment Methods in SPH. *International Journal of Ocean and Coastal Engineering* 2018; 1(02): 1840002.
38. Chiron L, Leffe dM, Oger G, Le Touzé D. Fast and accurate SPH modelling of 3D complex wall boundaries in viscous and non viscous flows. *Computer Physics Communications* 2019; 234: 93-111. doi: https://doi.org/10.1016/j.cpc.2018.08.001.

39. Robinson M, Ramaioli M, Luding S. Fluid–particle flow simulations using two-way-coupled mesoscale SPH–DEM and validation. *International Journal of Multiphase Flow* 2014; 59: 121-134. doi: https://doi.org/10.1016/j.ijmultiphaseflow.2013.11.003.
40. He Y, Bayly AE, Hassanpour A, Muller F, Wu K, Yang D. A GPU-based coupled SPH-DEM method for particle-fluid flow with free surfaces. *Powder Technology* 2018; 338: 548-562. doi: https://doi.org/10.1016/j.powtec.2018.07.043.
41. Sun X, Sakai M, Yamada Y. Three-dimensional simulation of a solid–liquid flow by the DEM–SPH method. *Journal of Computational Physics* 2013; 248: 147-176. doi: https://doi.org/10.1016/j.jcp.2013.04.019.
42. Jonsson P, Jonsén P, Andreasson P, Lundström TS, Hellström JGI. Modelling dam break evolution over a wet bed with smoothed particle hydrodynamics: A parameter study. *Engineering* 2015; 7(05): 248.
43. O'Sullivan C. *Particulate Discrete Element Modelling: A Geomechanics Perspective*. CRC Press . 2014.
44. Cundall PA. Distinct element models of rock and soil structure. *Analytical and Computational Methods in Engineering Rock Mechanics* 1987: 129-163.
45. Gui-rong L. *Smoothed Particle Hydrodynamics: A Meshfree Particle Method*. World Scientific Publishing Company . 2003.
46. Zheng J, An X, Huang M. GPU-based parallel algorithm for particle contact detection and its application in self-compacting concrete flow simulations. *Computers and Structures* 2012; 112-113: 193-204. doi: https://doi.org/10.1016/j.compstruc.2012.08.003.
47. Khayyer A, Gotoh H, Falahaty H, Shimizu Y. An enhanced ISPH–SPH coupled method for simulation of incompressible fluid–elastic structure interactions. *Computer Physics Communications* 2018; 232: 139-164. doi: https://doi.org/10.1016/j.cpc.2018.05.012.
48. Liu Mb, Shao Jr, Li Hq. Numerical simulation of hydroelastic problems with smoothed particle hydrodynamics method. *Journal of Hydrodynamics* 2013; 25(5): 673-682. doi: 10.1016/S1001-6058(13)60412-6.
49. Fourey G, Hermange C, Le Touzé D, Oger G. An efficient FSI coupling strategy between Smoothed Particle Hydrodynamics and Finite Element methods. *Computer Physics Communications* 2017; 217: 66-81. doi: https://doi.org/10.1016/j.cpc.2017.04.005.
50. Fakhimi A, Villegas T. Calibration of a discrete element model for rock failure envelope and tensile strength 2004: 383-390.

© 2021 by the authors. Licensee SCU, Ahvaz, Iran. This article is an open access article distributed under the terms and conditions of the Creative Commons Attribution 4.0 International (CC BY 4.0 license) (http://creativecommons.org/licenses/by/4.0/).